

# Chapter I

## Introduction

### Cryoelectron Tomography

Decades ago the paradigm for cellular components was the one-gene/one-protein model, where the activities of the cell were performed by independent proteins catalyzing second-order reactions as they diffused and rotated quickly through the cell[1]. Today we understand that it is more complicated. The cell is a factory with ordered and regulated assembly lines whose activities are performed by macromolecular assemblies that can rightly be called machines. An important goal is to understand what these machines consist of, how they work, and how to modify them to serve us. How to understand them? It would be simpler to focus on individual proteins because these machines are often labile complexes difficult to purify and difficult to study with more established techniques, however, it is crucial to study them as a whole and preferably in their cellular context. Cryoelectron tomography allows us to do that.

Existing techniques left a gap between low-resolution and high-resolution. Light microscopy can view whole and living cells but the resolution is limited to the wavelength, around 400 nm. NMR and X-ray crystallography can produce atomic resolution structures but are typically limited to smaller domains or monomers. X-ray crystallography also can produce atomic structures, but requires that the protein be crystallizable: The bigger and more flexible the object, the less likely it will crystallize. Macromolecular machines are definitely large and some are necessarily flexible.

Cryoelectron microscopy-based single particle analysis can produce medium resolution (7–30 Å) structures of large complexes and can tolerate some flexibility, but requires purified complexes. Loosely bound adaptor proteins can be lost in the purification. Cryoelectron tomography (CET) fills this gap. Individual cells and complexes can be reconstructed without averaging to resolutions reaching 40 to 50 Å.

CET is a relatively new technique that extends traditional transmission electron microscopy (TEM)[2-5]. The first application to prokaryotes was in 1998[6]. TEM has produced much of our information in cell biology starting from the 1940s[7], but it introduces artifacts to the sample that undermine confidence in fine details. Traditionally, in order to view biological samples in the vacuum of the electron microscope (EM), the samples had to be fixed, dehydrated, embedded in resin, sectioned with an ultramicrotome, and stained with heavy metals—a lengthy and error-prone procedure. CET preserves samples in a nearly life-like state because the samples are flash-frozen in a thin layer of liquid to produce transparent, vitreous ice. Were the samples thawed, many cells would still be alive. The samples are kept frozen in the microscope during imaging.

CET produces 3-D reconstructions instead of just 2-D TEM images. Tomography is an imaging strategy that produces 3-D tomograms of a sample from 2-D projections using any electromagnetic radiation like light, X-rays (e.g., CAT scans), or electrons. Light's wavelength is on the order of hundreds of nanometers; an X-ray's is on the order of ångstroms and an electron's is on the order of picometers. Electrons are superior to X-rays because of the high number of useful scattering events for each instance of radiation damage and because electrons can be focused[8]. In order to produce a

tomogram, a tilt-series must be collected—ideally from -90 degrees to 90 degrees with a fine increment, while preserving the imaging conditions throughout. To do so manually with an EM is too time-consuming, but with the introduction of modern instruments and automated data-collection in the last decade, CET is possible.

There are many factors to be adjusted to collect excellent data, most of which are determined by the chief problem with biological samples: their limited dose-tolerance. Beyond a radiation threshold of  $\sim 80\text{--}200$  electrons/ $\text{\AA}^2$ , organic compounds are destroyed and literally bubble within the ice. The maximum dose must be fractionated over the total number of images[9]. The number of images should not be too high, or else each image would receive an insufficient dose, nor should they be too low, or else insufficient information will be collected. The minimum number is determined by the Crowther criterion, where the tilt increment is equated to  $180^\circ$  multiplied by the desired resolution distance (i.e., the inverse of the resolution) and divided by the product of the object's diameter and  $\text{Pi}$ [6, 10]. The number of images is then determined by the maximum tilt range of the microscope's goniometer, which is typically  $\pm 70^\circ$ . The inability to collect over the full  $180^\circ$  results in the missing wedge problem where typically  $\sim 30\%$  of the information is missing, which results in features parallel to the sample plane being poorly resolved. The two factors governing the tilt increment are the sample diameter and the desired resolution. The greater the object's diameter and the better the desired resolution, the finer the increment and the more images needed, which, if taken too far, will lower the signal-to-noise ratio of each image and yield a useless reconstruction.

The object's diameter should be narrow not only to allow sufficient information to be collected, but to minimize the number of inelastic scattering events, which not only are

devoid of useful projection data, but also damage the sample. Like shooting a bullet into a forest—the greater the number of trees, the less likely a bullet will avoid a tree. For a microscope with an accelerating voltage of 300 keV, like the F30 Polara of the Jensen lab, the mean inelastic free path is 350 nm[11], which means the mean distance an electron will travel through a sample before causing an inelastic event is 350 nm. Samples should thus be narrower than that to produce excellent tomograms.

The desired resolution should be realistic in consideration of the object's diameter and is typically worse than 5 nm and even poorer for thicker samples[6, 12]. Given the expected resolution, one chooses the defocus and the magnification. The defocus' effect is much like an electromagnetic aperture, in a sense cutting off information past a certain resolution[13]. By removing noisier high-resolution information, the contrast is improved at the expense of lower resolution. (Contrast is the ratio of the difference in intensity of the foreground and background divided by the background intensity.) The defocus is set so that information past the desired resolution is affected. Since the data must be pixelated in order to use computational image processing and reconstruction, necessarily the limitations of discrete sampling must be considered. The limiting Nyquist resolution distance is twice the sampling[13], i.e., the pixel value—for example, a sampling of 13.4 Å/pixel would have a Nyquist resolution distance of 26.8 Å. Truly, the limiting resolution is two-thirds the Nyquist frequency, or in this example, 40 Å, because of non-ideal conditions. The magnification must be set high enough to achieve the desired resolution.

From the tilt series a reconstruction is calculated using a weighted back-projection algorithm[10]. If the data were collected well, the Fourier structure factors would have

been sampled finely enough to achieve the desired resolution. The tomogram might not be the final step because identical 3-D particles within multiple reconstructions can be computationally extracted, aligned, and averaged to produce structures with a better signal-to-noise ratio[14]. This was first done with an unknown cytoplasmic protein in 2003[15], and there are tens of additional examples to date—like surface and capsid proteins from HIV and other viruses[16-23], the nuclear pore complex[24], microtubules[25, 26], and the flagellar motor[27].

CET is relatively young, so improvements are still being made. Dual-axis tomography is a method that recovers some of the missing wedge information by tilting the sample in two orthogonal directions. This produces a missing pyramid that lacks less than half as much information. The Jensen lab advanced the technique by helping design and implement a dual-tilt cartridge which improves the resolution and decreases the degree of anisotropy (see Appendix A)[28]. A protocol was also written on the proper use of the Vitrobot (see Appendix B)[29].

## **Discoveries**

Armed with the powerful technique of CET, the goal of studying macromolecular machines in their cellular context or *in vitro* was achieved. Biological discoveries were made in three areas: (1) the quaternary structure of the octahedrally-cored, *E. coli* pyruvate dehydrogenase and 2-oxoglutarate dehydrogenase complexes (PDHC and OGDHC, respectively), described in Chapter II;[30] (2) the novel surface and periplasmic ultrastructure of the spirochete *Treponema primitia*, described in Chapter IV; and (3) the

structure of *in situ* flagellar motors from *T. primitia*[27], *Hylemonella gracilis*, *Caulobacter crescentus*, and *Vibrio cholerae*, described in Chapters III, V, and VI.

## **Pyruvate dehydrogenase and 2-Oxoglutarate dehydrogenase complexes**

PDHC and OGDHC were studied with CET because although there was some indication that the peripheral subunits E1 and E3 were separated by a gap from the core E2 complex, the reigning model of the complexes was the face/edge model[31]. 12 E1 dimers were thought to be bound directly to the 12 edges of the E2 octahedral (i.e., cubic) core, and 6 E3 dimers were thought to be bound directly to the 6 faces. The model was based on 3 lines of evidence: (1) stoichiometry results which gave chain ratios of E1:E2:E3 as 2:2:1, which matches the number of edges and faces of a cube;[32] (2) negatively-stained TEM images of the complex which appeared to have subunits bound directly to the core[33, 34]; and (3) scanning transmission electron microscopy (STEM) results of the radial masses of the full and partial complexes, which were interpreted as supportive of the face/edge model[35]. Previous attempts failed to obtain a 3-D structure of the two complexes using single particle analysis (SPA) of 2-D cryoelectron microscopy (CEM) images because it was concluded that the position of the subunits was too variable[36, 37]. SPA requires one or a few stable and reproducible conformations of an object in order to classify and average together similar particles[13].

Dual-axis tomography was used to reconstruct *in vitro* complexes using high doses and high defocuses in order to improve contrast. The paper describing the results was published in *Structure* in December, 2005, and is reproduced in Chapter II[30]. The chief biological discovery was that the subunits E1 and E3 are flexibly tethered 11 nm

from the corners of the E2 cubic core and are definitely not bound directly to the core. The technological advance was that domains as small as 80 kilodaltons (kDa) could be resolved (in the microscopic sense), though not to a high enough resolution to computationally fit in crystal structures. Also, in contrast to contemporary studies of the flexible antibody, which compensated for low defocuses and low doses with extensive denoising and enhancement[38], no denoising was used to visualize the PDHC and OGDHC complexes. The dual-axis reconstruction had enough contrast and resolution as is to make the discoveries. The insight is that rather than having the three enzymes unconnected and diffusing independently through the bacterial cell, nature has instead brought them all together to form an assembly line or machine so that the metabolites are effectively concentrated where they are produced and modified. Nature has produced two variants of the PDH complex: the octahedrally cored version present in a portion of the Bacterial kingdom, and the icosahedrally cored version present in the rest of the Bacteria and in Eukaryotes. All are similar in having an E2 core with one or both subunits flexibly tethered close by.

### **Ultrastructure of *Treponema primitia***

The second project was the ultrastructure of *Treponema primitia*. It is a member of the Phylum *Spirochaetes*, which are helical or undulate cells propelled by periplasmic, rather than external, flagella[39]. *T. primitia* lives in the hindgut of the termite *Zootermopsis angusticolis* and synthesizes acetate as a foodstuff for itself and its host from H<sub>2</sub> and CO<sub>2</sub>, which are intermediates produced during the fermentation of wood polysaccharides[40-42]. It was studied with CET, instead of the more commonly known

bacteria like *E. coli* or *Salmonella*, because it is 350 nm narrow, which is around the mean free inelastic path of the microscope, and because it participates with other microbes in the biotechnologically relevant process of biofuel production.

What was known of its ultrastructure and that of other spirochetes came from TEM images and non-cryo ET reconstructions, which revealed its two membranes, its periplasmic flagella, and, in one instance, cytoplasmic filaments[42-44]. Some termite gut spirochetes were found to definitely attach at their cell poles to neighboring protozoa, and in one case, actually help propel it[43, 45, 46]. Surface structures were a major finding in the author's CET reconstructions of *T. primitia*, and different kinds have been seen before in other cells. In general, surface structures serve as protective coatings, as platforms for adhesion and interaction with neighbors and hosts, and in motility[47]. S-layers are proteinaceous networks often packed in crystalline arrays[47] that act as an additional cell wall in Bacteria and Archaea. Unusual grappling-hook structures called "hami" tie together neighboring archaea in one species[48]. "Goblets," which actually resemble goblets, fully coat the surface of the bacteria *Flexibacter polymorphus*[49, 50]. Fibrils like pili and fimbriae may attach to other cells or surfaces, may transfer genetic information or serve in motility[51].

Three surface structures, two of them novel, and two novel periplasmic structures were discovered through CET reconstructions of *T. primitia*. Its flagellar motor was also well reconstructed, but will be discussed in the next section. Fibrils extended in one or two tufts from either cell pole for hundreds of nanometers. They may help the cells to attach to each other, other organisms, or surfaces. "Surface bowls" dotted, but did not fully cover, its outer membrane (OM). They appeared to be spread out mostly randomly,

except for one case where three rows of bowls spiraled around a portion of a cell. Rows of “surface hook arcades” wrapped around some cells. They formed a series of arches, and each arch was composed of two counteropposed hooks. The best guess for their function is to increase drag, which is essential for current models of spirochete motility and will be discussed later. At each tip were “periplasmic cones” that appeared to be porous-like and even maintained their cone shape in connected, undivided cells. The discovery of a second outer periplasmic layer (OPL), perhaps consisting of peptidoglycan, resolves the conundrum of how spirochetes can rotate their flagella inside the periplasm without rupturing or desupporting the outer membrane. Flagella (PF) were observed between the inner periplasmic layer (IPL) and the OPL. In the cytoplasm were membrane invaginations, 30 nm wide spherical bodies, a central zone free of ribosome-like particles that may be the nucleoid, and arrays near the tips under the inner membrane (IM) that may be chemotaxis arrays.

Spirochete motility models are complicated and untested, and the newly observed ultrastructure was reconciled with them. For *T. primitia*'s class of spirochete, it is believed that the rotation of the PF causes the outer sheath (OS), which is the OM and OPL, to rotate in one direction[52, 53]. The drag or shear of the OS provides the foothold for the protoplasmic cylinder (PC), which is the IM and IPL, and concomitantly, the attached PF and the OS, to counterrotate. The whole cell drills through gel-like viscous media and moves forward. See Chapter IV for a fuller discussion.

## ***In situ* flagellar motors**

The bacteria flagella motor is a fascinating macromolecular machine that can rotate at speeds between 3600 and 60000 rpm in various bacteria, and although it is slower than the 80,000 to 150,000 rpm speeds of a jet turbine, the flagella motor is even more remarkable for its ~ 50–70 nm size. It is a focus of active research because of its amazing ability to assemble itself, to rotate at high speeds, and to tolerate symmetry mismatch between all of its components. The motor has been reviewed extensively[54-57] and will be described briefly. The motor moves the bacteria by using either a proton or sodium concentration gradient to turn the propeller-like flagellar. The power-generating components of the motor are located in the inner membrane, and the shaft extends from there out through the peptidoglycan (PG) layer and outer membrane and connects to the several-micron-long flagella.

The motor is composed of more than 20 proteins and is assembled by an additional 30 (Figure I-1). The *Salmonella* and *E. coli* motors have been the most studied versions, and these cells have exterior flagella. The part of the motor proximal to the cell is called the basal body and comprises the most important components. The rotor is the first component to be assembled; it consists of ~ 26 copies of FliF, and has a mean symmetry of 25–26[58, 59] (Figure I-2). Bound to the rotor comes the same number of FliG proteins, to which are then attached the C ring[55]. The C ring resides in the cytoplasm just below the rotor and has a larger diameter than the rotor. The C ring has a mean symmetry of 34 and consists of approximately 34 copies of FliM and ~ 4 times as many copies of FliN[60, 61]. The C ring is the switchgear for the motor and causes the motor to rotate CCW or CW. Many more assembly proteins attach themselves to this

initial complex and create the export apparatus. Through it and atop the rotor is built the flagella rod or shaft, which has 11-fold helical symmetry. As the shaft rises, a hole is cut through the PG layer. Between this layer and the shaft many species then attach a bushing called the P ring, which is made from FlgI proteins. An additional bushing through the OM, called the L ring, is then made from FlgH proteins. As the shaft rises outwards, a hook is created to turn rotation motion into propeller motion, and finally the several-micron long flagella is built and eventually capped by a 5-fold symmetric complex. Sometime between the creation of the C ring and the capping of the flagella, several stators are assembled around the rotor and on top of the C ring. The stators convert the electro-chemical energy of the gradient into mechanical energy to turn the rotor. Each stator is thought to be composed of a complex of 4 MotA and 2 MotB proteins[62]. The maximum number of stator “studs” appears to be either 12 or 16 in various species.

The nearly occult numerology of the flagella motor, among other problems, has confused attempts to propose mechanisms[55, 63]. In *Salmonella* and *E. coli*, it is believed that the N-terminal portion of FliG attaches to the 26-fold symmetric rotor while its middle and C-terminal portions rest upon FliM of the 34-fold symmetric C-ring[64]. Some portion of FliG must tether the rotor to the C ring. The critical, rotation-generating interaction occurs between MotA’s charged, cytoplasmic domain and the complementarily charged domain of FliG (Figure 3)[56]. The difference of 8 between the symmetries of the rotor and stator, which equaled the estimated number of torque-generating units in resurrection studies of the stators[65], led to suggestions that the stators fit over the 8 unmatched FliM proteins. However, it is unlikely that MotA can

directly interact with FliM, and the variable symmetry of the C ring and rotor discourages models that rely on numerically-precise interactions[66]. The motor can probably tolerate a variety of numerical mismatches, which is remarkable for a machine. Human-made machines rely on precise interactions of gears and cogs. It is more likely that the MotA domains “walk” upon the FliG domains and that the number of gaps is insufficient to make enough MotA domains detach from the C ring[67]. The tethered rotor and its attached rod would then rotate along with the C ring.

Spirochetes contain many of the same components as other bacteria, with some minor differences. The sequenced *Borrelia* and *Treponema* species (*B. garinii*, *T. pallidum*, and *T. denticola*) do not have the FlgH L ring genes, as is expected since the flagella does not go through the OM, however, *Leptospira interrogans* does[57]. *Borrelia* and *Leptospira* have the FlgI P ring genes, but *Treponema*, curiously, do not[57]. This information is helpful for understanding what the alternative bushing is in *T. primitia*. Additionally, Blast searches found no genes for the P and L rings in *Firmicutes*, so perhaps they use the same bushing as *Treponema*. Since not much is known about the copy numbers of the components in Spirochetes, it is assumed that they are similar to *Salmonella* and *E. coli*.

Until two decades ago, our knowledge of the flagellar motor basal body came from 2-D TEM images[68-79] (Figure I-4). Only general features could be seen, and some approximate measurements were taken of the components. Most of our detailed information about the motor comes from single particle analysis of cryo-EM images of the *in vitro* *Salmonella* basal body[59, 60, 63, 80, 81]. The *Caulobacter crescentus* basal body without the C ring has also been reconstructed[82]. This technique necessarily must

study biochemically-isolated objects, which not only removes the rotor and such from its bacterial context, but also might remove loosely bound proteins. The *in situ* motor has been imaged using negatively stained, freeze-etched samples. The number of stator studs has been counted in such a way, and so has the *in situ* shape of the C ring, however, the images are 2-D, difficult to interpret, and measurements can only be estimated. Science has until recently had to settle for cartoons of the *in situ* motor.

*In situ* CET reconstructions of the flagellar motor from *T. primitia*, *Hylemonella gracilis*, *Caulobacter crescentus*, and *Vibrio cholerae* show the entire machine in its cellular context as if frozen in time. The chief discovery was the stators, which were revealed in 3-D for the first time. *T. primitia*'s structure was determined first. Its stators had strong 16-fold symmetry, but the studs were twenty times larger than that of the two OmpA domains of each stator complex. *H. gracilis*'s stator region had variable symmetry. Only the 13-fold class average showed stud density, and the volume of the studs was as expected. No stator symmetry was detectable in the others, but a stator ridge was visible in *C.c.* The diameter of the stator region was ~ 60, ~ 50 and ~ 40 nm in *T. primitia*, *H. gracilis*, and *C. caulobacter*, respectively, so there is variability in the diameters of flagellar motors across species. The C ring diameter matched the stator diameter, justifying the belief that the stators make crucial interactions with the C ring. Novel structures were seen in *T. primitia*: instead of a P ring, it had a P collar. Export apparatus shapes—i.e. a ring and what could be a ribosome—were found in nearly all motors under the rotor. An extended “E” collar was seen in *H. gracilis*, and the presence of a T ring was also found in *V. cholerae*, just as in *V. alginolyticus* (Figure I-3c)[83]. See Chapter VI for a more complete comparison of the motors. Each motor structure had

some unexpected difference in diameter or structure, so new discoveries will probably be made as the flagellar motors from other species are studied.

## References

1. Alberts, B. The cell as a collection of protein machines: preparing the next generation of molecular biologists. *Cell*. **92**, 291-4 (1998).
2. Jensen, G. J., and Briegel, A. How electron cryotomography is opening a new window onto prokaryotic ultrastructure. *Curr Opin Struct Biol*. **17**, 260-7 (2007).
3. Lucic, V., Forster, F., and Baumeister, W. Structural studies by electron tomography: from cells to molecules. *Annu Rev Biochem*. **74**, 833-65 (2005).
4. McIntosh, R., Nicastro, D., and Mastronarde, D. New views of cells in 3D: an introduction to electron tomography. *Trends Cell Biol*. **15**, 43-51 (2005).
5. Subramaniam, S., and Milne, J. L. Three-dimensional electron microscopy at molecular resolution. *Annu Rev Biophys Biomol Struct*. **33**, 141-55 (2004).
6. Grimm, R., et al. Electron tomography of ice-embedded prokaryotic cells. *Biophys J*. **74**, 1031-42 (1998).
7. Frey-Wyssling, A. The submicroscopic structure of the cytoplasm. *J R Microsc Soc* **60**, 128-139 (1940).
8. Henderson, R. The potential and limitations of neutrons, electrons and X-rays for atomic resolution microscopy of unstained biological molecules. *Q Rev Biophys* **28**, 171-193 (1995).

9. McEwen, B. F., Downing, K. H., and Glaeser, R. M. The relevance of dose-fractionation in tomography of radiation-sensitive specimens. *Ultramicroscopy*. **60**, 357-73 (1995).
10. Frank, J. *Electron Tomography*. Springer, New York (2006).
11. Grimm, R., Typke, D., Barmann, M., and Baumeister, W. Determination of the inelastic mean free path in ice by examination of tilted vesicles and automated most probable loss imaging. *Ultramicroscopy*. **63**, 169-79 (1996).
12. Koster, A. J., et al. Perspectives of molecular and cellular electron tomography. *J Struct Biol*. **120**, 276-308 (1997).
13. Frank, J. *Three-Dimensional Electron Microscopy of Macromolecular Assemblies*. Oxford University Press, Inc., New York (2006).
14. Walz, J., et al. Electron Tomography of Single Ice-Embedded Macromolecules: Three-Dimensional Alignment and Classification. *J Struct Biol*. **120**, 387-95 (1997).
15. Grunewald, K., Medalia, O., Gross, A., Steven, A. C., and Baumeister, W. Prospects of electron cryotomography to visualize macromolecular complexes inside cellular compartments: implications of crowding. *Biophys Chem*. **100**, 577-91 (2003).
16. Cardone, G., et al. Visualization of the herpes simplex virus portal in situ by cryo-electron tomography. *Virology* (2006).
17. Chang, J. T., Schmid, M. F., Rixon, F. J., and Chiu, W. Electron cryotomography reveals the portal in the herpesvirus capsid. *J Virol*. **81**, 2065-8 (2007).

18. Deng, B., O'Connor, C. M., Kedes, D. H., and Zhou, Z. H. Direct visualization of the putative portal in the Kaposi's sarcoma-associated herpesvirus capsid by cryoelectron tomography. *J Virol.* **81**, 3640-4 (2007).
19. Forster, F., Medalia, O., Zauberman, N., Baumeister, W., and Fass, D. Retrovirus envelope protein complex structure in situ studied by cryo-electron tomography. *Proc Natl Acad Sci U S A.* **102**, 4729-34 (2005).
20. Harris, A., et al. Influenza virus pleiomorphy characterized by cryoelectron tomography. *Proc Natl Acad Sci U S A.* **103**, 19123-7 (2006).
21. Zanetti, G., Briggs, J. A., Grunewald, K., Sattentau, Q. J., and Fuller, S. D. Cryo-Electron Tomographic Structure of an Immunodeficiency Virus Envelope Complex In Situ. *PLoS Pathog.* **2** (2006).
22. Zhu, P., et al. Electron tomography analysis of envelope glycoprotein trimers on HIV and simian immunodeficiency virus virions. *Proc Natl Acad Sci U S A.* **100**, 15812-7 (2003).
23. Zhu, P., et al. Distribution and three-dimensional structure of AIDS virus envelope spikes. *Nature.* **441**, 847-52 (2006).
24. Beck, M., et al. Nuclear pore complex structure and dynamics revealed by cryoelectron tomography. *Science.* **306**, 1387-90 (2004).
25. Garvalov, B. K., et al. Luminal particles within cellular microtubules. *J Cell Biol.* **174**, 759-65 (2006).
26. Nicastro, D., McIntosh, J. R., and Baumeister, W. 3D structure of eukaryotic flagella in a quiescent state revealed by cryo-electron tomography. *Proc Natl Acad Sci U S A.* **102**, 15889-94 (2005).

27. Murphy, G. E., Leadbetter, J. R., and Jensen, G. J. In situ structure of the complete *Treponema primitia* flagellar motor. *Nature*. **442**, 1062-4 (2006).
28. Iancu, C. V., et al. A "flip-flop" rotation stage for routine dual-axis electron cryotomography. *J Struct Biol*. **151**, 288-97 (2005).
29. Iancu, C. V., et al. Electron cryotomography sample preparation using the Vitrobot. *Nat Protoc*. **1**, 2813-9 (2006).
30. Murphy, G. E., and Jensen, G. J. Electron cryotomography of the *E. coli* pyruvate and 2-oxoglutarate dehydrogenase complexes. *Structure*. **13**, 1765-73 (2005).
31. de Kok, A., Hengeveld, A. F., Martin, A., and Westphal, A. H. The pyruvate dehydrogenase multi-enzyme complex from Gram-negative bacteria. *Biochim Biophys Acta*. **1385**, 353-66 (1998).
32. Reed, L. J., et al. Reconstitution of the *Escherichia coli* pyruvate dehydrogenase complex. *Proc Natl Acad Sci U S A*. **72**, 3068-72 (1975).
33. Bleile, D. M., Munk, P., Oliver, R. M., and Reed, L. J. Subunit structure of dihydrolipoyl transacetylase component of pyruvate dehydrogenase complex from *Escherichia coli*. *Proc Natl Acad Sci U S A*. **76**, 4385-9 (1979).
34. Oliver, R. M., and Reed, L. J. Multienzyme Complexes in *Electron Microscopy of Proteins*. (Harris, R., ed.), Academic Press, London, (1982).
35. Yang, H. C., Hainfeld, J. F., Wall, J. S., and Frey, P. A. Quaternary structure of pyruvate dehydrogenase complex from *Escherichia coli*. *J Biol Chem*. **260**, 16049-51 (1985).

36. Wagenknecht, T., Grassucci, R., Berkowitz, J., and Forneris, C. Configuration of interdomain linkers in pyruvate dehydrogenase complex of *Escherichia coli* as determined by cryoelectron microscopy. *J Struct Biol.* **109**, 70-7 (1992).
37. Wagenknecht, T., Grassucci, R., and Schaak, D. Cryoelectron microscopy of frozen-hydrated alpha-ketoacid dehydrogenase complexes from *Escherichia coli*. *J Biol Chem.* **265**, 22402-8 (1990).
38. Sandin, S., Ofverstedt, L. G., Wikstrom, A. C., Wrangé, O., and Skoglund, U. Structure and flexibility of individual immunoglobulin G molecules in solution. *Structure.* **12**, 409-15 (2004).
39. Li, C., Motaleb, M. A., Sal, M., Goldstein, S. F., and Charon, N. W. Gyration, rotations, periplasmic flagella: the biology of spirochete motility in *The Spirochetes Molecular and Cellular Biology*. (Saier, M. H., Jr & Garcia-Lara, J., eds.), Horizon Press, Norfolk (2001).
40. Breznak, J. A., and Switzer, J. M. Acetate synthesis from H<sub>2</sub> plus CO<sub>2</sub> by termite gut microbes. *Appl Environ Microbiol.* **52**, 623-630 (1986).
41. Graber, J. R., Leadbetter, J. R., and Breznak, J. A. Description of *Treponema azotonutricium* sp. nov. and *Treponema primitia* sp. nov., the first spirochetes isolated from termite guts. *Appl Environ Microbiol.* **70**, 1315-20 (2004).
42. Leadbetter, J. R., Schmidt, T. M., Graber, J. R., and Breznak, J. A. Acetogenesis from H<sub>2</sub> plus CO<sub>2</sub> by spirochetes from termite guts. *Science.* **283**, 686-9 (1999).
43. Holt, S. C. Anatomy and chemistry of spirochetes. *Microbiol Rev.* **42**, 114-60 (1978).

44. Izard, J., et al. Tomographic reconstruction of treponemal cytoplasmic filaments reveals novel bridging and anchoring components. *Mol Microbiol.* **51**, 609-18 (2004).
45. Bloodgood, R. A., and Fitzharris, T. P. Specific associations of prokaryotes with symbiotic flagellate protozoa from the hindgut of the termite *Reticulitermes* and the wood-eating roach *Cryptocercus*. *Cytobios.* **17**, 103-22 (1976).
46. Cleveland, L. R., and Grimstone, A. V. The fine structure of the flagellate *Mixotricha paradoxa* and its associated micro-organisms. *Proc Roy Soc London.* **B159**, 668-686 (1964).
47. Fernandez, L. A., and Berenguer, J. Secretion and assembly of regular surface structures in Gram-negative bacteria. *FEMS Microbiol Rev.* **24**, 21-44 (2000).
48. Moissl, C., Rachel, R., Briegel, A., Engelhardt, H., and Huber, R. The unique structure of archaeal 'hami', highly complex cell appendages with nano-grappling hooks. *Mol Microbiol.* **56**, 361-70 (2005).
49. Ridgway, H. F. Ultrastructural characterization of goblet-shaped particles from the cell wall of *Flexibacter polymorphus*. *Can J Microbiol.* **23**, 1201-13 (1977).
50. Ridgway, H. F., Wagner, R. M., Dawsey, W. T., and Lewin, R. A. Fine structure of the cell envelope layers of *Flexibacter polymorphus*. *Can J Microbiol.* **21**, 1733-50 (1975).
51. White, D. *The Physiology and Biochemistry of Prokaryotes*. Oxford University Press, New York (2007).
52. Berg, H. C. How spirochetes may swim. *J Theor Biol.* **56**, 269-73 (1976).

53. Berg, H. C., and Turner, L. Movement of microorganisms in viscous environments. *Nature*. **278**, 349-51 (1979).
54. Berg, H. C. The rotary motor of bacterial flagella. *Annu Rev Biochem*. **72**, 19-54 (2003).
55. Kojima, S., and Blair, D. F. The bacterial flagellar motor: structure and function of a complex molecular machine. *Int Rev Cytol*. **233**, 93-134 (2004).
56. Blair, D. F. Flagellar movement driven by proton translocation. *FEBS Lett*. **545**, 86-95 (2003).
57. Limberger, R. J. The periplasmic flagellum of spirochetes. *J Mol Microbiol Biotechnol*. **7**, 30-40 (2004).
58. Suzuki, H., Yonekura, K., and Namba, K. Structure of the rotor of the bacterial flagellar motor revealed by electron cryomicroscopy and single-particle image analysis. *J Mol Biol*. **337**, 105-13 (2004).
59. Thomas, D. R., Francis, N. R., Xu, C., and DeRosier, D. J. The three-dimensional structure of the flagellar rotor from a clockwise-locked mutant of *Salmonella enterica* serovar Typhimurium. *J Bacteriol*. **188**, 7039-48 (2006).
60. Young, H. S., Dang, H., Lai, Y., DeRosier, D. J., and Khan, S. Variable symmetry in *Salmonella typhimurium* flagellar motors. *Biophys J*. **84**, 571-7 (2003).
61. Brown, P. N., Mathews, M. A., Joss, L. A., Hill, C. P., and Blair, D. F. Crystal structure of the flagellar rotor protein FliN from *Thermotoga maritima*. *J Bacteriol*. **187**, 2890-902 (2005).

62. Braun, T. F., Al-Mawsawi, L. Q., Kojima, S., and Blair, D. F. Arrangement of core membrane segments in the MotA/MotB proton-channel complex of *Escherichia coli*. *Biochemistry*. **43**, 35-45 (2004).
63. Thomas, D. R., Morgan, D. G., and DeRosier, D. J. Rotational symmetry of the C ring and a mechanism for the flagellar rotary motor. *Proc Natl Acad Sci U S A*. **96**, 10134-9 (1999).
64. Brown, P. N., Terrazas, M., Paul, K., and Blair, D. F. Mutational analysis of the flagellar protein FliG: sites of interaction with FliM and implications for organization of the switch complex. *J Bacteriol*. **189**, 305-12 (2007).
65. Blair, D. F., and Berg, H. C. Restoration of torque in defective flagellar motors. *Science*. **242**, 1678-81 (1988).
66. Thomas, D., Morgan, D. G., and DeRosier, D. J. Structures of bacterial flagellar motors from two FliF-FliG gene fusion mutants. *J Bacteriol*. **183**, 6404-12 (2001).
67. Manson, M. D. How 34 pegs fit into 26 + 8 holes in the flagellar motor. *J Bacteriol*. **189**, 291-3 (2007).
68. Abram, D., Vatter, A. E., and Koffler, H. Attachment and structural features of flagella of certain bacilli. *J Bacteriol*. **91**, 2045-68 (1966).
69. Coulton, J. W., and Murray, R. G. Cell envelope associations of *Aquaspirillum serpens* flagella. *J Bacteriol*. **136**, 1037-49 (1978).
70. Holt, S. C., and Canale-Parola, E. Fine structure of *Spirochaeta stenostrepta*, a free-living, anaerobic spirochete. *J Bacteriol*. **96**, 822-35 (1968).

71. Hovind-Hougen, K., Birch-Andersen, A., and Jensen, H. J. Ultrastructure of cells of *Treponema pertenu* obtained from experimentally infected hamsters. *Acta Pathol Microbiol Scand [B]*. **84**, 101-8 (1976).
72. Jackson, S., and Black, S. H. Ultrastructure of *Treponema pallidum* Nichols following lysis by physical and chemical methods. II. Axial filaments. *Arch Mikrobiol.* **76**, 325-40 (1971).
73. Khan, S., Dapice, M., and Reese, T. S. Effects of *mot* gene expression on the structure of the flagellar motor. *J Mol Biol.* **202**, 575-84 (1988).
74. Khan, S., Ivey, D. M., and Krulwich, T. A. Membrane ultrastructure of alkaliphilic *Bacillus* species studied by rapid-freeze electron microscopy. *J Bacteriol.* **174**, 5123-6 (1992).
75. Khan, S., Khan, I. H., and Reese, T. S. New structural features of the flagellar base in *Salmonella typhimurium* revealed by rapid-freeze electron microscopy. *J Bacteriol.* **173**, 2888-96 (1991).
76. Khan, S., Zhao, R. B., and Reese, T. S. Architectural features of the *Salmonella typhimurium* flagellar motor switch revealed by disrupted C-rings. *Journal Of Structural Biology.* **122**, 311-319 (1998).
77. Kupper, J., Wildhaber, I., Gao, Z., and Baeuerlein, E. Basal-body-associated disks are additional structural elements of the flagellar apparatus isolated from *Wolinella succinogenes*. *J Bacteriol.* **171**, 2803-10 (1989).
78. Nauman, R. K., Holt, S. C., and Cox, C. D. Purification, ultrastructure, and composition of axial filaments from *Leptospira*. *J Bacteriol.* **98**, 264-80 (1969).

79. Paster, B. J., and Canale-Parola, E. Involvement of periplasmic fibrils in motility of spirochetes. *J Bacteriol.* **141**, 359-64 (1980).
80. Francis, N. R., Sosinsky, G. E., Thomas, D., and DeRosier, D. J. Isolation, characterization and structure of bacterial flagellar motors containing the switch complex. *J Mol Biol.* **235**, 1261-70 (1994).
81. Sosinsky, G. E., Francis, N. R., Stallmeyer, M. J., and DeRosier, D. J. Substructure of the flagellar basal body of *Salmonella typhimurium*. *J Mol Biol.* **223**, 171-84 (1992).
82. Stallmeyer, M. J., Hahnenberger, K. M., Sosinsky, G. E., Shapiro, L., and DeRosier, D. J. Image reconstruction of the flagellar basal body of *Caulobacter crescentus*. *J Mol Biol.* **205**, 511-8 (1989).
83. Terashima, H., Fukuoka, H., Yakushi, T., Kojima, S., and Homma, M. The *Vibrio* motor proteins, MotX and MotY, are associated with the basal body of Na-driven flagella and required for stator formation. *Mol Microbiol.* **62**, 1170-80 (2006).

## Figures

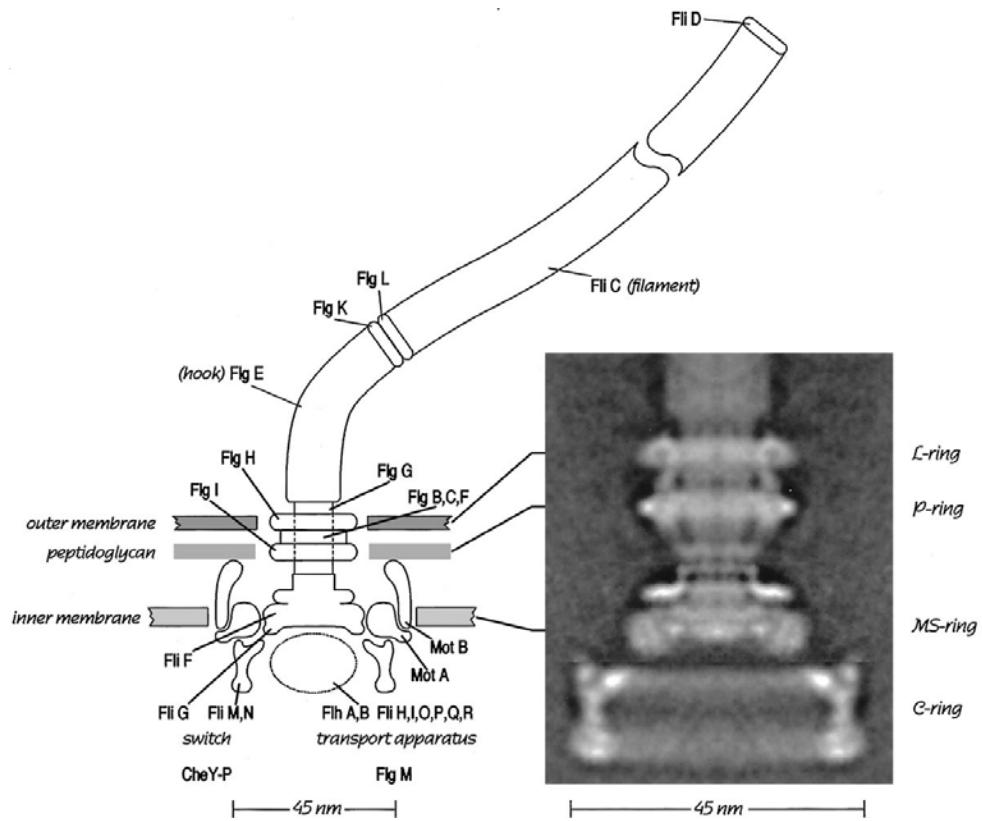


**Figure I-1 Components of the flagellar motor**

from Berg, HC, *Annu. Rev. Biochem.*, 2003[54]

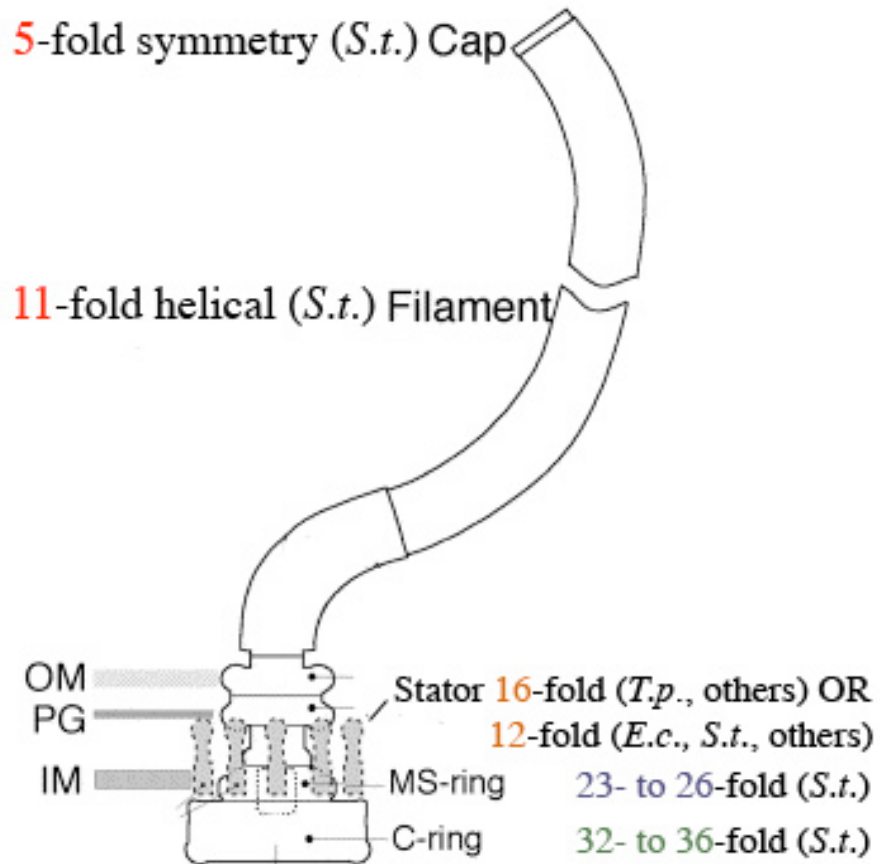


**Figure I-2 Symmetry of motor components**

modified from Blair, D.F., FEBS, 2003[56]

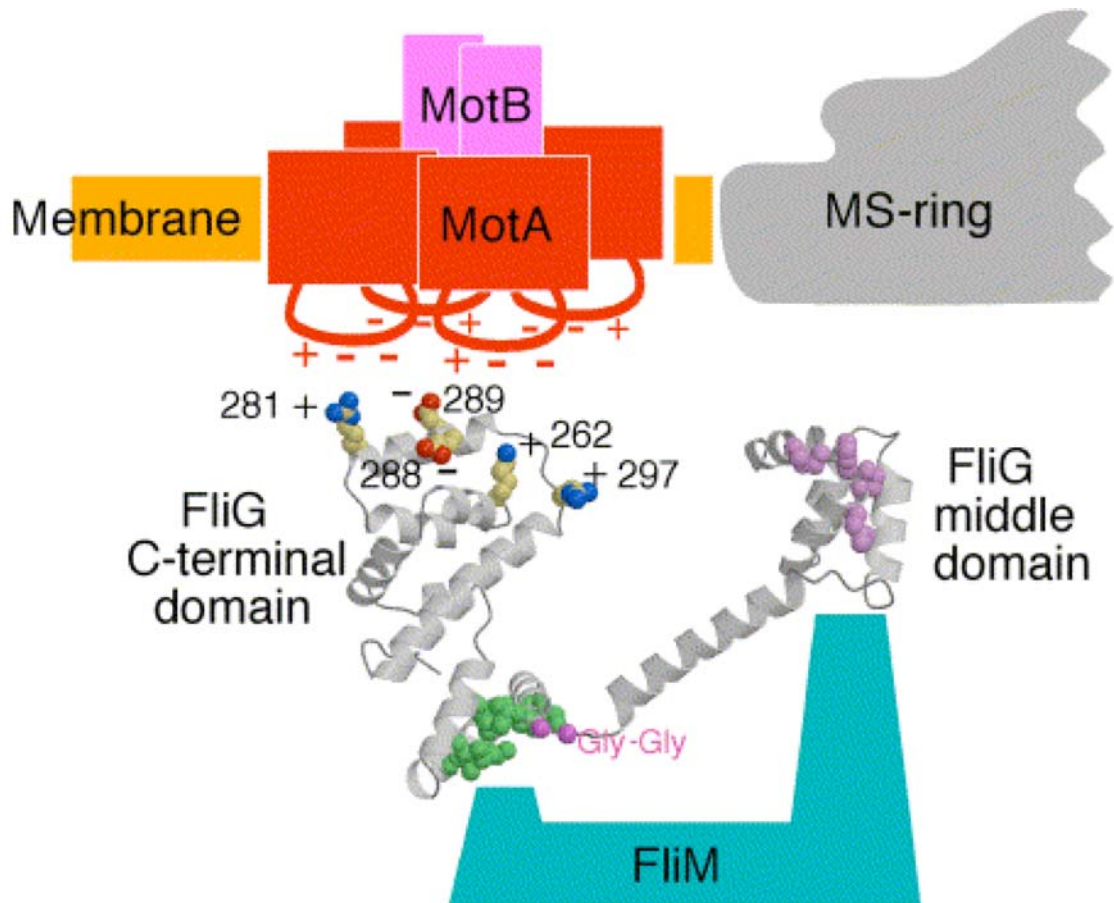


**Figure I-3 Stator-C ring interaction**

from Blair, D.F. FEBS, 2003[56]

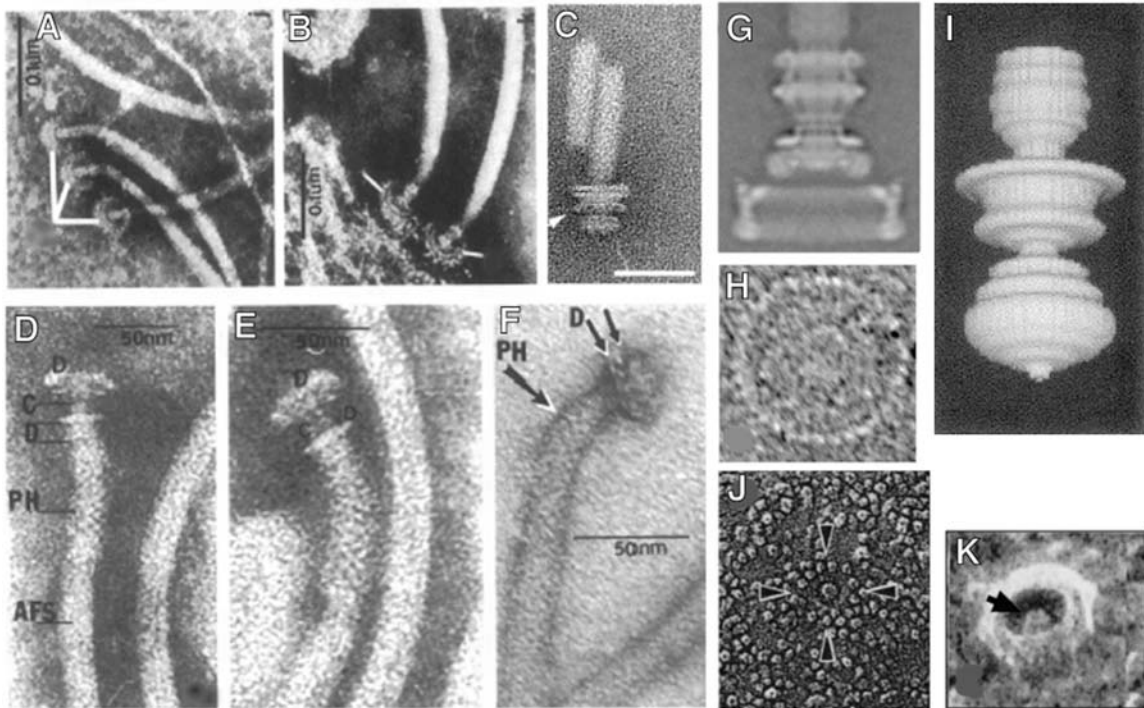


**Figure I-4 Past electron microscopy of flagellar motors *in vitro* and *in situ***

(A–B) Negatively stained EM images of the *Treponema pallidum* basal body. (Panels A,B,D–F are from Holt, S.C., 1978[43].) (C) The *Vibrio alginolyticus* basal body. The arrowhead points to the novel T ring. (From Terashima, H., et al., 2006[83].) (D–E) The *Leptospira interrogans* basal body. (F) The *Spirochaeta stenostrepta* basal body. (G) Cryo EM reconstruction of the *Salmonella* basal body. (Panels G, H, J and K are from Blair, D.F., FEBS, 2003[56].) (H) Cryo EM image of the C ring from *Salmonella*. (I) The reconstructed *Caulobacter crescentus* basal body. (From Stallmeyer, M.J., et al., 1989[82].) (J) Negatively stained freeze-etch image of an *in situ* flagellar motor. (K) Negatively stained freeze-etch of a C ring from an *in situ* flagellar motor.